Focusing Effects of Teleseismic Wavefields by the Subducting Plate beneath Cascadia: Evidence for Slab Continuity

Guanning Pang[1*], Geoffrey A. Abers[1], Peter E. van Keken[2]

[1]Dept. of Earth and Atmospheric Sciences, Cornell University, Ithaca, NY 14850, USA
[2]Earth and Planets Laboratory, Carnegie Institution for Science, Washington DC 20015, USA
*Corresponding author: gp327@cornell.edu

Abstract

Seismic wave amplitudes have tremendous sensitivity to subduction structure; however, they are affected by attenuation, scattering and focusing, and have therefore been sparsely used compared with traveltimes. We measure and model teleseismic body wave amplitudes recorded at a dense broadband array in the Washington Cascades (iMUSH). These data show anomalous amplitude variations with complex azimuthal dependence at the low frequency of 0.05 Hz, accompanied by significant multipathing. We demonstrate using spectral-element numerical simulations that focusing of the teleseismic wavefield by the Juan de Fuca slab is responsible for some of the amplitude anomalies. The focusing effects can contaminate the apparent differential attenuation measurements and produce at least 20% of the inferred attenuation signal. The focusing results in complex azimuthal patterns that produce different phase and amplitude variations than does intrinsic attenuation, which should allow separation of elastic (focusing) and anelastic effects. Our results indicate that the amplitudes are sensitive to the subducting slab geometry and subduction structure, and can be used to refine seismic images. Ubiquitous focusing effects are

observed along the arc, suggesting a continuous Juan de Fuca slab from Canada to northern California.

Keywords: Focusing/defocusing; Cascadia subduction zone; Teleseismic attenuation; Slab hole

1. Introduction

Seismic imaging provides critical information on the structure of subduction zones. While seismic velocities images based on travel times are sensitive to the petrologic composition (e.g., Cai et al., 2018; Guo et al., 2021), seismic attenuation provides independent constraints with greater sensitivity to thermal structure and melt fraction (e.g., Abers et al., 2014; Takei, 2017; Wei and Wiens, 2020). Recent developments in measuring differential attenuation from teleseismic body waves provide comparable resolution to local seismic attenuation imaging in subduction zones (Eilon and Abers, 2017; Soto Castaneda et al., 2021). However, focusing effects can significantly impact the frequency content of seismic waveforms and levels comparable to intrinsic attenuation. For example, Ford et al. (2012) estimated an apparent differential attenuation operator (Δt^*) of 0.1–0.4 s between *S* and *ScS* from focusing as described by velocity anomalies, contributing significantly to their observed differential t^* of -4–+2s. Chaves and Ritsema (2016) found that the focusing due to long-wavelength velocity perturbations in the mantle can explain the anomalies in amplitude ratios of the phases *ScS* and ScS_2 without involving variations in shear wave attenuation. The issue is that seismic amplitude variations have tremendous sensitivities to the elastic structure and not just attenuation, and can potentially be used to place constraints on wavespeeds beyond what travel times allow (e.g., Dalton & Ekström, 2006; Lin et al., 2012; Song & Helmberger, 2007; Tang et al., 2014).

Several studies have shown that teleseismic waves are influenced by the high-velocity slabs and exhibit amplitude anomalies due to focusing (e.g., Suetsugu, 1999; Vidale, 1987). Three-dimensional ray tracing indicates that amplitudes of teleseismic waves are sensitive to the velocity structure of the subducted slab, and can be used to constrain the slab geometry and its depth extent (Pankow & Lay, 2002). By modeling the shear wave amplitude patterns resulting from focusing, Pankow et al. (2002) detected the presence of metastable olivine in deep slabs that were ambiguous from seismic travel-time tomography. Zhan et al. (2014) modeled the multi-pathing features of the teleseismic waveforms and refined the slab structure beneath the Sea of Okhotsk.

A few studies also use the amplitudes of the teleseismic wave to refine the structure on the receiver side. Song & Helmberger (2007) used systematic waveform distortions to constrain the sharpness of the fast slab-like structure beneath the western edge of the Great Plains of North America. Tang et al. (2014) observed significant amplitude variations in teleseismic wavefield across the Changbaishan volcanic complex of northeast China. By modeling the amplitude variations, they obtained a better constraint on the slow velocity anomalies at the transition zone depths, which were not well recovered by travel-time tomography.

Although the incoming teleseismic wave amplitudes have tremendous sensitivity to near-receiver structure, using focusing effects of teleseismic waves to probe the slab structure near the receiver is less common. In this study, we analyze the amplitude patterns at the period of ~2–20s for teleseismic waveforms recorded at the imaging Magma Under Mount St. Helens (iMUSH) broadband seismic array (Creager, 2014; Mann et al., 2019), to explore the focusing effects of teleseismic wavefields by the Juan de Fuca slab. We compare the observed amplitude variations to those of synthetic seismograms from multiple Juan de Fuca slab models, to show that focusing is responsible for large parts of the observed amplitude variation at 20 s period. Then, we estimate the contributions of the slab focusing to differential attenuation measurements using teleseismic waveforms, following Eilon & Abers (2017). These comparisons show a strong effect of slab focusing at low frequency, and reveal properties that distinguish attenuation from focusing. We also demonstrate the continuity of Juan de Fuca slab by examining amplitude variations at 20 s using broadband stations near the arc.

2. Data and Method

We examine data from the iMUSH broadband seismic array deployed between June 2014 and August 2016. iMUSH comprised 70 broadband three-component seismometers arranged in a circular patch within 50 km of the Mount St. Helens (MSH) edifice, at ~10 km spacing (Fig. 1). We searched the gCMT catalog (*www.globalcmt.org*; Ekström et al., 2012) for earthquakes with magnitude ≥ M_w 6 that occurred at 30° – 70° from the iMUSH array. We obtained viable data for 32 earthquakes from June 2014 to August 2016; four occurred at the Aleutian subduction zone, five near Japan, 21 in Latin America, one near Greenland, and one in the Atlantic Ocean (Fig. 1). To fill the gap in the southwest, we extended the searching distance to 90° from the iMUSH and acquired 19 earthquakes in the Tonga–Fiji area, recognizing that *S* and *SKS* may interfere at these distances.

We remove the instrument response from the three-component seismic waveforms, and rotate signals to the radial (R) and transverse (T) components. We apply a narrowband filter at a center frequency of 0.05 Hz (20 s period) to waveforms and retained waveforms with signal-noise-ratios (SNR) ≥ 10 (Fig. 2a). Then, we measure the *S* amplitudes on R and T components for earthquakes at distances of 30–70°. We only measure *S* amplitudes from T components for earthquakes from Tonga-Fiji to minimize the impact of *SKS* energy. Using these criteria, 23 earthquakes are used in further amplitude variation analysis (Fig. 1; Table S1). Among the 23 earthquakes, 11 earthquakes are east to southeast of the Cascadia subduction zone, four earthquakes are located in Tonga-Fiji, four earthquakes are in the Aleutian-Alaska subduction zone, and four are near Hokkaido, Japan (Fig. 1; Table S1).

Differential attenuation using teleseismic waveforms provides constraints on structure (e.g., Eilon and Abers, 2017; Soto Castaneda et al., 2021). We applied the multi-narrow filter technique to measure amplitude ratios ($A_{ij}(f)$) and phase shift ($\Delta\phi_{ij}(f)$) between neighboring stations i and j at frequency f. Assuming no frequency dependency, $ln(A_{ij}(f))$ will vary linearly with f with a slope that is directly proportional to the differential integrated attenuation (Δt^*). Similarly, $\Delta\phi_{ij}(f)$ is linearly related to $ln(f)$ with a slope that is proportional to Δt^*. Therefore, Δt^* for each station can be determined by fitting A_{ij} and $\Delta\phi_{ij}$ spectra via linear least-square inversion. The multi-narrow filter technique, based on Eilon and Abers (2017), is described in more detail in the supplementary information.

3. Amplitude anomaly

3.1. Long-period amplitude variations

The teleseismic wavefields at the period of ~20 s show significant variation in amplitudes across the iMUSH array. Figure 2a shows the filtered *S* waveforms recorded at stations ME03 (hereafter referred as to Sta 1) and MK11 (hereafter referred as to Sta 2) for the earthquake located near Greenland at a back azimuth of ~48°. The amplitude at Sta 2 is 1.7 times the waveform amplitude at Sta 1 at 20 s period (Fig. 2a). Figure 2b shows the *S*-wave amplitudes of the Greenland earthquake relative to the median amplitude on the iMUSH stations. The amplitude measurements show significant variations in the direction perpendicular to wave propagation direction with greater amplitudes at the stations located southeast of MSH, resulting in an apparent "striping" pattern with stripes subparallel to the wave propagation direction (Fig. 2b; Fig. S1). The pattern resembles those seen in surface waves due to focusing and multipathing (e.g., Forsyth & Li, 2005; Lin et al., 2012). The largest amplitude is ~2.5 larger than the weakest amplitude.

Earthquakes in the Atlantic Ocean with back azimuths of ~82° show similar spatial variation patterns with the greatest amplitudes east of MSH (Fig. 2c; Fig. S1); the strongest amplitude is about 2.5 times the weakest amplitude. The amplitudes gradually decrease from east to west (Fig. 2c; Fig. S1). These patterns, with gradients parallel to wave propagation. However, amplitudes of teleseismic waveforms arriving from back azimuths of ~130° decrease monotonically in the direction of wave propagation, from southeast to northwest, with amplitudes changing up to 2.5 times (Fig. S2). This back azimuth is almost normal to the arc and propagates in an up-dip direction, suggesting that the amplitude anomaly results from slab structure.

Seismic wavefields from earthquakes at western back azimuths differ with weaker variations compared to those from eastern back azimuths. Amplitude measurements for earthquakes near Tong–Fiji at back azimuths of ~230° show amplitude gradients perpendicular to the wave propagation direction with the greatest amplitudes northwest of MSH (Fig. S2). We observe minor amplitude variations from earthquakes at Alaska-Aleutian with back azimuths ~298°. The amplitudes are 10% weaker at $x \approx 40$ km (Fig. 2d and Fig. S2). Similarly, there is no apparent variation pattern in amplitudes of earthquakes near Hokkaido, Japan (Fig. S2).

Overall, the amplitude variation patterns depend on the teleseismic wave incident direction in a complicated manner. Amplitudes decrease from east to west in a factor of ~2 for seismic waves coming from eastern back azimuths (Fig. 2b and 2c; Fig. S1 and S2). On the contrary, for seismic waves with western back azimuths, the amplitude variation is minor with slightly lower amplitudes at stations east of MSH (Fig. 2d and Fig. S2). Stations west of MSH have large amplitudes if the teleseismic waves come from southwestern back azimuths perpendicular to subducting direction of the Juan de Fuca slab (Fig. S2).

We exclude mantle wedge attenuation as the origin of the amplitude anomalies because of the low frequencies involved: for typical values of differential *S*-wave attenuation and mantle wedge path lengths (e.g., Eilon & Abers, 2017), amplitude variations in 0.05 Hz signals should be <20%, not >100%. Furthermore, higher attenuation would be expected at the east of MSH because of the higher temperature in the mantle backarc than forearc. These variations should be relatively independent of wave propagation direction if mantle-wedge attenuation was the source; the wedge is at 40−70 km depth immediately below MSH (Mann et al., 2019) so teleseismic *S* waves arriving at the easternmost stations should sample the hot wedge regardless of back azimuth. We also rule out a local amplification effect, again because of the strong azimuth dependence in the amplitude variations. The azimuth dependence suggests that these amplitude anomalies can be attributed to the focusing of the Juan de Fuca slab.

3.2 Slowness analysis

To further understand deviations of these signals from global models, we calculate the slowness power spectrum of the teleseismic *S* wavefields (See supplement for details). Figure 3 shows the frequency-wave number (*f*-*k*) analysis for the earthquake in the Atlantic Ocean shown in Fig. 2c, which shows significant amplitude anomalies. The *S* wave energy in the first 25 s has a different slowness azimuth than the *S* energy after 20 s lag (Fig. 3), about 5 s/° lower (faster) rotated in azimuth 15° counterclockwise (Fig. 3). By comparison, *S* waves for an Alaska-Aleutian earthquake without significant amplitude anomalies shows insignificant changes in slowness vectors with lag time (Fig. S3). To further confirm the observed changes in slowness vectors, we apply a sliding window slowness analysis to the first 60 s of the *S* waves, with 20 s long windows that are shifted in 10 s increments. This process yields ray parameter and back azimuth as a function of time (Fig. S4). We observe significant differences in slowness and back azimuth for the Atlantic Ocean earthquake while the slowness vectors of the Alaska earthquake show no change (Fig. S4). This pattern differs from that of most array recordings of teleseismic body waves, which show insignificant deviations from great-circle paths and radial Earth predictions in the 30-90° distance range (e.g., Filson, 1975).

The *f-k* procedure is repeated for 17 earthquakes with ten earthquakes at eastern back azimuths and seven earthquakes in Alaska–Japan region at back azimuths of ~300° (We do not use any Tonga-Fiji earthquakes because the *S* wave amplitude decreases to noise levels 10 s after the *S* picks). We observed systematic differences between eastern and western back azimuths. Slowness vectors of the eastern earthquakes rotate significantly between the *S* onset and signals 20 seconds later (Fig. 3). Earthquakes at western back azimuths show no change in slowness vectors. Two earthquakes at 48° and 60° from iMUSH near Japan have relatively larger slowness difference of 1.3 s/°. However, the slowness power spectrum for the earthquake at 48° distance has much poorer resolution due to the low SNR in the second window. We observe a strong anomalous phase 40 s after the *S* arrival for the earthquake at distance of 60°, which could be interference of the shear-coupled *PL* waves (Baag & Langston, 1985).

The slowness differences are consistent with the long-period amplitude variations in that earthquakes with strong amplitude anomalies have significant slowness anomalies, suggesting that the amplitude anomalies may result from the interference of two body waves propagating from slightly different directions for geometries propagating updip along the Juan de Fuca slab.

3.3. Apparent attenuation

To estimate apparent body-wave attenuation, we apply the multi-narrow filter technique similar to that of Eilon & Abers (2017) to *S* waves recorded on the T component, and then determine station-specific Δt^* estimates (see Supplement for details). Figure 4 presents the Δt^* at each station determined from three earthquakes, two from eastern back-azimuths and one from a western back-azimuth. Station-specific Δt^* estimates for earthquakes at eastern back-azimuths show clear large positive values of ~1.5 s (high attenuation) near MSH (-25 km $< x <$ 25 km; Fig 4a and 4b). The Δt^* estimates become negative, indicating larger high-frequency energy, at $x >$ 25 km. By contrast, Δt^* estimates for an earthquake at the western back-azimuth have large positive (high attenuation) values southwest of MSH and negative values northeast of MSH (Fig. 4c). The significant difference in Δt^* spatial patterns between eastern and western back-azimuths cannot be explained solely by the attenuation or local amplification for reasons discussed above, so are attributed to focusing by the Juan de Fuca slab.

4. Modeling slab-induced focusing and defocusing

To investigate the focusing effects, we calculate amplitude variations due to the high-velocity subducted slabs in synthetic waveforms generated with spectral–element method package SPECFEM2D (Tromp et al., 2008). We simulate the wave propagation up to 0.5 Hz, which is computationally expensive for global 3D simulation. For simplicity, we model an upgoing planar wave propagating along with the 2D model of the Cascadia subduction zone. We create the model for a slice along the Juan de Fuca slab downdip direction (black arrow in Fig. 1).

We explore amplitude variations resulting from three subduction models: Model i), a simplified Cascadia subduction zone model with a constant-velocity plate that is 10 % faster than the background mantle; Model ii), a theoretical Cascadia model based a thermal model tuned to the Washington Cascades and assuming a dry mantle wedge; and Model iii), the same theoretical Cascadia model but assuming a fully hydrated mantle wedge where temperatures are low enough to allow hydrous phases (Abers et al., 2017). We use GMSH (Geuzaine & Remacle, 2009) to define the 2–D finite element mesh. The size of the finite element ranges in 0.7 – 3.2 km. The fine elements allow the frequency contents to be well resolved up to 1 Hz. The region is small compared with curvature of the teleseismic wavefront at distances of 30°–90°, so the teleseismic wavefront can be considered as planar. The source is a Ricker wavelet with a central frequency of 0.5 Hz to generate an initial incident *SH* plane wave, starting ~150 km beneath the MSH at an incident angle of 25°. We simulate the seismic wavefields in two propagation scenarios: 1. The initial plane wave is incident from the lower right corner (east) of the model to the iMUSH array (Fig. 5), and 2. the initial plane wave is incident from the lower left (west) of the model to the iMUSH array. We investigate amplitude anomalies purely due to the focusing effects of the high-velocity slab and we do not include any intrinsic attenuation.

We apply a similar multi-narrow-filter technique to the synthetic seismograms as with real data (section 3.3) to estimate the apparent Δt^* in three ways: 1. Using the $A_{ij}(f)$

measurements only; 2. Using the $\Delta\phi_{ij}(f)$ measurements only; 3. Using $A_{ij}(f)$ and $\Delta\phi_{ij}(f)$ simultaneously. Please see Supplement for more details.

4.1 Simplified slab model (Model i)

We start with a simplified Cascadia model (Model i), composed of a ~35 km thick high–velocity slab subducting into a homogeneous background mantle, consistent with the thermal thickness of an 8–10 Ma Juan de Fuca plate (Fig. 5). The slab geometry was obtained from array-based receiver function imaging (Mann et al., 2019) integrated with active-source constraints updip (Parsons et al., 1998) and deeper body-wave tomographic imaging (Schmandt & Humphreys, 2010). We use a *P*-wave velocity (V_p) of 8.6 km/s and *S*-wave velocity (V_s) of 4.7 km/s for the subducting slab; V_p of 7.8 km/s, and V_s of 4.1 km/s for the background mantle. The background mantle velocities are consistent with active-source and ambient-noise constraints beneath the back-arc (Delph et al., 2018; Parsons et al., 1998). The 10% step between the slab and background mantle, while globally high (e.g., Lay, 1997), provides an illustration of maximum potential focusing effects. We use a uniform density of 3.4 g/cm^3 for both subducting slab and mantle (Fig. 5). We also generate synthetic seismograms for a slab-free, homogenous velocity model. By comparing the synthetic seismograms between Model (i) and the homogeneous model, we can ensure that any observed amplitude anomalies in the synthetic seismograms are not due to computational effects.

Figure 6a shows the raw synthetic seismograms at Sta 1 and Sta 2. The synthetic seismograms show significant variations in amplitudes, comparable to actual data at 0.05 Hz. The amplitude of the raw waveform in Sta 2 is about three times the waveform amplitude in Sta 1 (Fig. 6a). The amplitude changes are substantial in frequencies 0.05–0.5 Hz, as shown in the amplitude spectra (Fig. 6b; Fig. S5). Differences with the amplitude spectra generated from the homogeneous model suggest that these amplitude changes are attributed to the focusing and multi-pathing effects of the high-velocity slab (Fig. S5). Next, we bandpass-filtered the synthetic seismograms using the same 0.05-Hz narrow-band filter used in the observations (Fig. 2). The spatial variation of the synthetic wavefield exhibits broad similarity to observations for events from eastern back azimuths, which show east-west variations of a factor of 1.5 (Fig. 2; Fig. 6c; Fig. S1 and S2). Furthermore, the modeled amplitude spectra illustrate apparent frequency-dependent amplitude changes in 0.05–0.5 Hz (Fig. 6b; Fig. S5). A Δt_{12}^{*} of 0.45 s was obtained by fitting the spectral ratios at 0.05–0.5 Hz (Fig 6b), suggesting that the focusing effects by the slab may bias the differential attenuation Δt^{*} measurement from teleseismic wavefields.

Figure 7 shows examples of $A_{ij}(f)$ and $\Delta\phi_{ij}(f)$ measurements of the narrowband filter comb. Amplitudes at Sta 1 are smaller than the amplitudes at Sta 2 at 0.05–0.5 Hz (Fig. 6b). The amplitude ratio spectra are similar to theoretical amplitude spectra resulting from intrinsic attenuation, such that a Δt_{12}^{*} of 0.43 s was obtained by fitting to the amplitude ratio spectra (Fig. 7a, Eq. S1). Similarly, the phase difference $\Delta\phi_{12}(f)$ measurements between Sta 1 and Sta 2 are well modeled by frequency-independent differential attenuation operator (Eq. S3); however, it is important to note that a larger Δt_{12}^{*} of 0.73 s was obtained from the phase spectra (Fig. 7b), larger than the Δt_{ij}^{*} derived from fitting amplitude. For intrinsic attenuation, fitting phase spectra separately should result in similar Δt_{ij}^{*}, but no such constraint exists for focusing effects.

Not all $A_{ij}(f)$ and $\Delta\phi_{ij}(f)$ can be well described by differential attenuation (Eq. S1 and S3). For example, A_{34} and $\Delta\phi_{34}$ measurements between station MO06 (hereafter referred as to Sta 3; Fig. 1) and ML09 (hereafter referred as to Sta 4; Fig. 1) show non-linear variations in frequencies. Amplitudes at Sta 3 are weaker than the amplitudes at Sta 4 at long periods (Fig. 6c and 7a), but at frequencies above 0.2 Hz, the amplitude ratio increases as frequencies increase, resulting in a negative Δt_{34}^{*} of -0.47 s (Fig. 7a). The Δt_{34}^{*} of 1.0 s from $\Delta\phi_{34}$ is positive, unlike the amplitude-based measurement, and is much larger (Fig. 7b). We also fit the linear portions of amplitude and phase shift spectra up to only 0.2 Hz, which is closer to the upper limit used in real data. We obtained a Δt_{34}^{*} of 1.47 s by fitting the amplitude ratio spectra; however, this value is larger than the 1.06 s from phase shift spectra. Overall, there is an apparent inconsistency between amplitude and phase and a generally poor fit to the intrinsic attenuation model predictions.

Figure 8 presents station-specific Δt_i^{*} measurements for amplitude only, phase only, and both. The Δt_i^{*} values exhibit significant variations in all three cases. Δt_i^{*} values inferred from $A_{ij}(f)$ measurements range from -0.3 s to +0.3 s with significant variations at the east of MSH (Fig. 8a). Δt_i^{*} values inferred from $\Delta\phi_{ij}(f)$ are higher than those from A_{ij} in a range of -1.1 s to +0.6 s, with three distinguishing stripes going north-south (Fig. 8b). The spatial pattern of Δt_i^{*} inferred from joint inversion of $A_{ij}(f)$ and $\Delta\phi_{ij}(f)$ is an eclectic mix of the patterns when doing the inversion separately, and depends on the weighting (γ) between $A_{ij}(f)$ and $\Delta\phi_{ij}(f)$. With twice weights on the amplitude ratios, the Δt_i^{*} is in -0.4–+0.3 s with similar spatial variations to the amplitude-derived estimates (Fig. 8c).

We also calculate the amplitude variation when the initial plane wave is incident from the lower left corner (west) at an incident angle of 25°. These seismic wavefields show no apparent amplitude variations in the synthetic seismograms (Fig. 6d-f). Similar to observations for earthquakes at back azimuth of ~300°, amplitudes at 0.05 Hz show some minor variations that stations at $x \approx 40$ km record slightly weaker wavefields by ~10% (Fig. 2d, Fig. 6f, Fig. S1 and S2). We apply the multi-narrow-band filter technique to estimate the Δt^{*} values (Fig. 7c and 7d).

The Δt_i^* (~-0.04–+0.08 s) determined from $\Delta\phi_{ij}(f)$ is slightly larger than those derived from $A_{ij}(f)$ in -0.02–+0.01 s (Fig. 8d-e). However, both these estimates are negligible.

In summary, focusing of the subducted slab exhibits apparent back-azimuth dependence. The focusing for the teleseismic waves at the western back azimuth is negligible. On the contrary, focusing for eastern back azimuths can produce differential Δt_i^* for S waves of at least 0.3 s (Fig. 8), which is about 20% of the absolute values of the observed Δt_i^* at iMUSH (Fig. 4) and could translate to large and spurrious attenuation anomalies if not accounted for.

4.2 Dry wedge model (Model ii)

We implement a more geodynamically realistic Cascadia subduction zone model to further explore focusing effects (Fig. 9a). The wavespeed model is derived from a thermal model and consistent mineralogy using the approach and parameters described elsewhere (Abers et al., 2017; Connolly, 2005; van Keken et al., 2011, 2018;). Wavespeeds are then predicted from this thermo-petrologic model (Abers & Hacker 2016). The thermal model is similar to the Cascadia model published, with full description, in Syracuse et al. (2010) but using following modifications: i) the geometry of the slab surface described above in Section 4.1; ii) 33.4 mm/yr convergence rate; iii) 8 Ma ocean lithosphere age at the trench. We excluded radiogenic heat production in the overriding crust within 300 km from the trench to account for the gabbroic nature of the Siletzia terrane (Wada and Wang, 2009; Wells et al., 2014). As in van Keken et al. (2011), we start slab-wedge coupling at 80 km depth. The model heat flow closely matches available heat flow data (e.g., Salmi et al. 2017). In this simulation, the slab and mantle wedge are assumed to be anhydrous everywhere.

Similar to the synthetic waveforms from Model i, we observe frequency-dependent amplitude variations across the iMUSH array for waves arriving from eastern back azimuths (Fig. S6). The amplitudes at 0.05 Hz manifest a similar spatial pattern to the observation and the simulation of Model i (Fig. 9b), reinforcing the interpretation of the amplitude variation resulting from the focusing effects of the high-velocity slab. We measured the $A_{ij}(f)$ and $\Delta\phi_{ij}(f)$ measurements and determined the station-specific Δt_i^* values using the same procedure as we did to Model i. Similar to Model i, the $A_{ij}(f)$ and $\Delta\phi_{ij}(f)$ measurements share one of the two properties: $\Delta\phi_{ij}(f)$ measurements give a larger Δt_{ij}^* than the $A_{ij}(f)$ measurements, or they are not linearly related to f or $ln(f)$ (Fig. S7a-b). Station-specific Δt_i^* determined from $A_{ij}(f)$ measurements has positive values of ~0.05 s in between x = -25 km and 25 km and negative values of ~ -0.1 s at x < -25 km and x > 25 km (Fig. S8a). Δt_i^* determined from $\Delta\phi_{ij}(f)$ has similar sign variations along the east-west direction but with a larger range of values of -0.26–+0.16 s (Fig. S8b). The Δt_i^* obtained from joint inversion of $A_{ij}(f)$ and $\Delta\phi_{ij}(f)$ are in the range of -0.14–+0.06 s with the same spatial variation pattern along the east-west direction (Fig. S8c).

There is no clear amplitude variation in the long-period synthetic waveforms if the plane wave is incident from the west (Fig. S9), consistent with the results of Model i and observations. The estimated Δt^* is also minor, in range of -0.04–+0.05 s, with weak negative Δt^* in x = -25 – 25 km (Fig. S8d-f). In contrast, the focusing of the Model ii produce differential Δt_i^* with similar spatial variation to that observed for the earthquakes at the eastern back-azimuths (Fig. 4a–b and S8a–c). Depending on the weight of phase-shift data, the contribution to Δt_i^* of focusing/defocusing effects can be up to 20%.

4.3 Hydrated wedge model (Model iii)

We explore a third Cascadia subduction model, similar to Model ii but assuming that the forearc mantle wedge is fully hydrated, as has been suggested for the Cascadia forearc (Abers et al., 2017; Bostock et al., 2002). Hydrous minerals are stable where forearc temperatures are less than ~800°C, resulting in substantially lower wavespeeds in the upper mantle of the overriding plate (Fig. 9c).

For the incident wavefield from the eastern back azimuth, an insignificant variation in the amplitude at 0.05 Hz is observed for Model iii (Fig. 9d). Stations within 10 km from MSH in the east-west direction tend to have slightly weaker amplitude than the stations farther from MSH. However, the difference is minor. Significant amplitude variations are observed at higher frequencies (Fig. S6). Similar to the results of Model i and ii, $A_{ij}(f)$ and $\Delta\phi_{ij}(f)$ measurements deviate from linear proportionalities with respect to f and $ln(f)$, respectively (Fig. S7c-d). Station-specific Δt_i^* determined from $A_{ij}(f)$ show complicated spatial variation patterns. Stations at x = -50 km have significantly variable Δt_i^* measurements from -0.25 s to +0.1 s (Fig. S10a). Stations at x = -25–10 km have positive Δt_i^* of 0.1–0.15 s (Fig. S10a). Δt_i^* values change to ~0.0s at x = 10 km and gradually decrease to -0.1 s with x increasing to 50 km (Fig. S10a). Δt_i^* inferred from $\Delta\phi_{ij}(f)$ measurements vary over a larger range. Stations in x = -25 – 25 km observe large positive Δt_i^* of ~0.3 s while stations at x < -25 km and x > 25 km have negative Δt_i^* of -0.5 – -0.3 s (Fig. S10b). Similarly, joint inversion of $A_{ij}(f)$ and $\Delta\phi_{ij}(f)$ results in a spatial striping pattern with Δt_i^* in range of -0.34–+0.17 s (Fig. S10c).

The spatial variation of Δt_i^* is similar to the Δt_i^* variation from Model ii but over a larger range. The contributions of focusing are 10%–30% of observed range for earthquakes at eastern back-azimuths, depending on the relative weight between the amplitude and phase data.

For the model earthquake from western back azimuths, long-period (20 s) wavefields show subtle variations in amplitudes (Fig. S9). Stations within 25 km of MSH have slightly larger amplitudes (Fig. S9). A larger negative Δt^* in the range of -0.16 – +0.23 s was obtained values at x = 0–40 km (Fig. S10d–f), unlike Models i and ii. These predictions are up to ~20% of those observed (Fig. 4c; Fig. S10d–f), depending on the relative weight between the amplitude and phase data.

5. Discussion

5.1. *Amplitude focusing and structure beneath the iMUSH array*

The spectral-element numerical simulations have shown that teleseismic *S*-wave amplitude variations at 0.05 Hz can be interpreted as focusing effects of the Juan de Fuca high-velocity subducted slab. Models i and ii can produce the observed amplitude anomalies in teleseismic wavefields, supporting the idea of focusing effects as the origin of the observed amplitude variation. The ratios between the strongest and weakest amplitudes of the synthetic seismograms are 1.5 and 1.3 for Model i and Model ii, respectively. Both ratios are somewhat smaller than the observed ratios of ~2 at teleseismic body waves. The thermal models (ii and iii) include temperature- and hydration-dependent effects on mantle wavespeed, but do not include sharp boundaries such as associated with subducting crust that would further focus wavefields in the manner of Model i. Hence, it is likely that the velocity contrasts in Models ii and iii underestimate focusing, so are not sufficient to produce enough focusing to reproduce the amplitude variations observed. Slab geometry could play another critical role in wavefield focusing not considered here. Chu et al. (2012) proposed that the Juan de Fuca slab has a thickness of 60 km and is subducted to a depth of 100 km beneath the Portland region, from a mixture of tomography and waveform modeling. We investigated the amplitude variations in the synthetic seismograms from the slab thickness of ~60 km (Fig. S11). We obtained a similar amplitude pattern at 0.05 Hz as Model i but with the ratio of strongest to weakest amplitude enlarged to 1.8 (Fig. S11), close to that observed. Since increasing the slab thickness yields better recovery of amplitude variations, it is possible that the thickness of the high-velocity Juan de Fuca slab may be greater at greater depth. As a final test, we test whether very deep structure (>150 km depth) creates additional amplitude anomalies. To do so, we started the incident wave at greater depths (~200km below MSH) than described above using Model ii, where the slab thickness gets larger with increasing depth. However, we did not observe a change in amplitude variations, so the amplitude variation does not seem sensitive to structure at a depth > 150 km.

The observed amplitude anomalies may involve complicated 3D multi-pathing effects, as indicated by beamforming (Fig. 3). Multi-pathing effects are well documented in surface wave studies, which show that the interference of two plane waves incoming from slightly different directions results in interference or striping patterns in amplitude with gradients perpendicular to the great circle path (e.g., Forsyth & Li, 2005; Lin et al., 2012). Maeda et al. (2011) observed a similar interference pattern in the recovered wavefields from the Hi-Net array in Japan at a period of 20–50 s. They found two signals incoming at slightly different slowness, interfering to produce the observed Moiré pattern. In Cascadia, the multi-pathing interference from the *f-k* analysis could contribute to the striping patterns of amplitude variations for earthquakes at eastern back azimuths (Fig. 2, Fig. S1 and S2). Beamforming indicates that the *S* waves from eastern back azimuths come from slightly different directions at different time lags (Fig. 3 and Fig. S4), demonstrating that some energy comes in off the great circle. Ray bending by the high-velocity slab could create such ray-path distortion. Such distortion is rare; in typical continental arrays the teleseismic body waves (30–90° distance) arrive within error at the slowness predicted by simple global models (e.g., Filson, 1975). These slowness anomalies indicate that amplitude variations are likely due to the combinations of interference and focusing effects.

Such focusing has a direct effect on apparent differential attenuation. The Δt^* measurements show strong azimuthal dependence, which varies strongly with event back-azimuth in a manner similar to low-frequency focusing (Fig. 7–8, Fig. S8–S10). Unlike what is expected for intrinsic attenuation, the Δt^* estimated from phase shift measurements are more significant than the Δt^* estimated from the amplitude ratios, and sometimes differ in sign. The absolute value of predicted Δt^* from focusing can be 0.3–1.2 s, which is large and comparable to the observed Δt^* measurements (Fig. 4, Fig. 8). Corrections need to be applied to the differential attenuation measurements before any valid interpretation in the Cascadia attenuation structures can be made. That said, the strong azimuthal dependence and relatively small effects from some back-azimuths suggest that careful comparison of back azimuth patterns, as well as amplitude and phase, should allow separation of focusing and attenuation.

Previous studies of the forearc show that the Moho disappears west of the MSH (Bostock et al., 2002; Mann et al., 2019), observations that are consistent with the highly hydrated mantle wedge. However, our results favor a relatively cold and dry overlying mantle wedge of the Cascade subduction zone because Model ii can reproduce the observed amplitude variation pattern better than Model iii, although the amplitude variations are much smaller than observed (Fig. 9). One possibility is that crustal rather than mantle structure controls the disappearance of the mantle; shear wave structure from ambient noise studies indicates that large lateral changes in upper-plate crustal velocities are larger than due to serpentinization in the wedge (Crosbie et al., 2019). Comparison with Model i suggests that a more detailed characterization of this region, including sharp boundaries around thin layers of subducting crust and sediment, could significantly increase the amplitude anomalies, resolving the discrepancy. However, the very small scale of the relevant features (1–7 km) presents challenges to the modest computational approach taken here.

5.2 Amplitude Evidence for Slab Continuity in Cascadia

Previous studies based on travel-time tomography have proposed a hole or tear in the Juan de Fuca slab near south of MSH at roughly 44°N to 46°N (Fig. 10) (e.g., Hawley & Allen, 2019; Schmandt & Humphreys, 2010). The proposed existence of this slab hole provided an explanation for the origin of MSH and nearby volcanic centers, offset tens of km west from the main volcanic front, as coming from below the young Juan de Fuca plate through the hole (Leeman et al., 2005). However, other studies argue that the hole is an artifact from reduced velocities in the mantle wedge (Roth et al., 2008; Mann et al., 2019). The amplitude variations of teleseismic *S* waves at ~20 s along the arc can resolve the continuity of the Juan de Fuca slab. Calibration of amplitude effects from iMUSH, where the wavefield is oversampled and shows clear patterns, allows interpretation of amplitudes all along the Cascades arc, where similar wavefields should be encountered if the slab structure is similar along strike. In particular, large amplifications at low frequencies (0.05 Hz) should be observed near and east of the arc for eastern back azimuths but not western back azimuths.

To test the existence of the slab hole, we examine amplitudes variation at 20 s period (0.05 Hz) using broadband stations near the arc along its entire length (Fig. 10). We focus on two earthquakes with large signal throughout the arc: one earthquake from the Aleutians at a western back azimuth (Fig. 1 and Fig. 2d) and from the Atlantic at an eastern back-azimuth (Fig. 1 and

Fig. 2c). We observe little variation in amplitudes and phases for the waveforms from the western back azimuth (Fig. 10a and Fig. S12). By contrast, waveforms from the eastern back azimuth significantly amplified by twice east of the arc with apparent phase shifts of ~2 sec (Fig. 10b and Fig. S12), similar to the observations at iMUSH (Fig. 2). Importantly, stations between 44°N and 46°N show an amplitude variation pattern identical to the pattern observed in iMUSH, suggesting strong slab focusing effects in the region (Fig. 2 and Fig. 10). The observed focusing suggests a high-velocity slab is continuous beneath and behind the arc and cannot be easily reconciled with the proposed slab hole. The ubiquitous focus effects along the arc suggest that the Juan de Fuca slab is continuous all the way from Canada to northern California without a major tear (Fig. 10). More generally, these results show that wavefield amplitudes can be used to extrapolate slab geometry to many places where intermediate-depth seismicity may be absent.

6. Conclusion

We observe amplitude anomalies with complex azimuthal patterns in long-period teleseismic body waves at the Cascadia subduction zone. These patterns can be interpreted as focusing and multipathing by the Juan de Fuca high-velocity slab. Focusing effects are first order for teleseismic body waves at frequencies as low as 0.05 Hz, which show strong amplification and off-great-circle arrivals for signals propagating updip. Teleseismic body-wave attenuation measurements can in some ways resemble focusing, but with different sensitivity to phase and amplitude variations. Focusing always results in complex azimuthal patterns, which are not always present in attenuation measurements particularly for shallow sources.

Our study shows that amplitudes of teleseismic body waves have great sensitivity to subducting slab structure. The amplitude information provides additional and tighter constraints on slab geometry. This study points to the potential power of full-waveform inversion, where amplitude as well as phase are considered, to refine the subduction zone structures. Based on the ubiquitous focus effects along the arc, we conclude that the Juan de Fuca slab is continuous from Canada to northern California.

Data Availability Statement

The iMUSH seismic data used in this study are available from the Incorporated Research Institutions for Seismology (IRIS; *www.iris.edu*) with the XD 2014-16 network code (https://doi.org/10.7914/SN/XD_2014). Modeling via SPECFEM2D is openly available via https://github.com/geodynamics/specfem2d. The code for array processing is available online on https://github.com/gnpang/gPar.

Acknowledgments

We thank Dr. Michael E. Mann for discussions about the Cascadia slab geometry, Dr. Zach Eilon for helping understanding body-wave attenuation measurements, and Dr. Wenbo Wu and Dr. Benjamin Baker for helping in SPECFEM2D simulation. Portions of this work are supported by National Science Foundation award EAR-1948834 (GA).

Reference

Abers, G. A., Fischer, K. M., Hirth, G., Wiens, D. A., Plank, T., Holtzman, B. K., McCarthy C. & Gazel, E. (2014). Reconciling mantle attenuation-temperature relationships from seismology, petrology, and laboratory measurements. *Geochemistry, Geophysics, Geosystems*, 15(9), 3521–3542.

Abers, G. A., & Hacker, B. R. (2016). A MATLAB toolbox and Excel workbook for calculating the densities, seismic wave speeds, and major element composition of minerals and rocks at pressure and temperature. *Geochemistry, Geophysics, Geosystems*, 17(2), 616–624.

Abers, G. A., van Keken, P. E., & Hacker, B. R. (2017). The cold and relatively dry nature of mantle forearcs in subduction zones. *Nature Geoscience*, 10(5), 333–337.

Baag, C. E., & Langston, C. A. (1985). Shear-coupled PL. *Geophysical Journal International*, 80(2), 363–385.

Bostock, M. G., Hyndman, R. D., Rondenay, S., & Peacock, S. M. (2002). An inverted continental Moho and serpentinization of the forearc mantle. Nature, 417(6888), 536–538.

Cai, C., Wiens, D. A., Shen, W., & Eimer, M. (2018). Water input into the Mariana subduction zone estimated from ocean-bottom seismic data. *Nature*, 563(7731), 389–392.

Chaves, C. A., & Ritsema, J. (2016). The influence of shear-velocity heterogeneity on ScS_2/ScS amplitude ratios and estimates of Q in the mantle. *Geophysical Research Letters*, 43(15), 7997–8005.

Chu, R., Schmandt, B., & Helmberger, D. V. (2012). Juan de Fuca subduction zone from a mixture of tomography and waveform modeling. *Journal of Geophysical Research: Solid Earth*, 117(B3), B03304.

Connolly, J. A. (2005). Computation of phase equilibria by linear programming: a tool for geodynamic modeling and its application to subduction zone decarbonation. *Earth and Planetary Science Letters*, 236(1-2), 524–541.

Creager, K. (2014). Collaborative Research: Illuminating the architecture of the greater Mount St. Helens magmatic systems from slab to surface [Data set]. International Federation of Digital Seismograph Networks. https://doi.org/10.7914/SN/XD_2014.

Crosbie, K. J., Abers, G. A., Mann, M. E., Janiszewski, H. A., Creager, K. C., Ulberg, C. W., & Moran, S. C. (2019). Shear velocity structure from ambient noise and teleseismic surface wave tomography in the cascades around Mount St. Helens. *Journal of Geophysical Research: Solid Earth*, 124(8), 8358–8375.

Dalton, C. A., & Ekström, G. (2006). Constraints on global maps of phase velocity from surface-wave amplitudes. *Geophysical Journal International*, 167(2), 820–826.

Delph, J. R., Levander, A., & Niu, F. (2018). Fluid controls on the heterogeneous seismic characteristics of the Cascadia margin. *Geophysical Research Letters*, 45(20), 11021–11029.

Ekström, G., Nettles, M., & Dziewoński, A. M. (2012). The global CMT project 2004–2010: Centroid-moment tensors for 13,017 earthquakes. *Physics of the Earth and Planetary Interiors*, 200, 1–9.

Eilon, Z. C., & Abers, G. A. (2017). High seismic attenuation at a mid-ocean ridge reveals the distribution of deep melt. *Science advances*, 3(5), e1602829.

Filson, J. (1975). Array seismology. *Annual Review of Earth and Planetary Sciences*, 3, 157–181.

Ford, S. R., Garnero, E. J., & Thorne, M. S. (2012). Differential t* measurements via instantaneous frequency matching: observations of lower mantle shear attenuation heterogeneity beneath western Central America. *Geophysical Journal International*, 189(1), 513–523.

Forsyth, D. W., & Li, A. (2005). Array analysis of two-dimensional variations in surface wave phase velocity and azimuthal anisotropy in the presence of multipathing interference. In *Seismic Earth: Array Analysis of Broadband Seismograms*, Eds. Levander, A. & Nolet, G. (Vol. 157, pp. 81–97). Washington DC: AGU.

Geuzaine, C., & Remacle, J. F. (2009). Gmsh: A 3-D finite element mesh generator with built-in pre-and post-processing facilities. *International Journal for Numerical Methods in Engineering*, 79(11), 1309–1331.

Guo, H., McGuire, J. J., & Zhang, H. (2021). Correlation of porosity variations and rheological transitions on the southern Cascadia megathrust. *Nature Geoscience*, 14(5), 341–348.

Hawley, W. B., & Allen, R. M. (2019). The fragmented death of the Farallon plate. *Geophysical Research Letters*, 46(13), 7386–7394.

Kennett, B. L., Engdahl, E. R., & Buland, R. (1995). Constraints on seismic velocities in the Earth from traveltimes. *Geophysical Journal International*, 122(1), 108–124.

Lay, T. (1997). Structure and Fate of Subducting Slabs, 185pp, San Diego CA: Academic Press.

Leeman, W. P., Lewis, J. F., Evarts, R. C., Conrey, R. M., & Streck, M. J. (2005). Petrologic constraints on the thermal structure of the Cascades arc. *Journal of Volcanology and Geothermal Research*, 140(1–3), 67–105.

Lin, F. C., Tsai, V. C., & Ritzwoller, M. H. (2012). The local amplification of surface waves: A new observable to constrain elastic velocities, density, and anelastic attenuation. *Journal of Geophysical Research: Solid Earth*, 117(B6), B06302.

Maeda, T., Obara, K., Furumura, T., & Saito, T. (2011). Interference of long-period seismic wavefield observed by the dense Hi-net array in Japan. *Journal of Geophysical Research: Solid Earth*, 116(B10), B10303.

Mann, M. E., Abers, G. A., Crosbie, K., Creager, K., Ulberg, C., Moran, S., & Rondenay, S. (2019). Imaging subduction beneath Mount St. Helens: Implications for slab dehydration and magma transport. *Geophysical Research Letters*, 46(6), 3163–3171.

McCrory, P. A., Blair, J. L., Waldhauser, F., & Oppenheimer, D. H. (2012). Juan de Fuca slab geometry and its relation to Wadati-Benioff zone seismicity. *Journal of Geophysical Research: Solid Earth*, 117(B9), B09306.

Pankow, K. L., & Lay, T. (2002). Modeling S wave amplitude patterns for events in the Kurile slab using three-dimensional Gaussian beams. *Journal of Geophysical Research: Solid Earth*, 107(B8), Art. No. 2167.

Pankow, K. L., Williams, Q., & Lay, T. (2002). Using shear wave amplitude patterns to detect metastable olivine in subducted slabs. *Journal of Geophysical Research: Solid Earth*, 107(B6), Art. No. 2108.

Parsons, T., Trehu, A. M., Luetgert, J. H., Miller, K., Kilbride, F., Wells, R. E., ... & Christensen, N. I. (1998). A new view into the Cascadia subduction zone and volcanic arc: Implications for earthquake hazards along the Washington margin. *Geology*, 26(3), 199–202.

Roth, J. B., Fouch, M. J., James, D. E., & Carlson, R. W. (2008). Three–dimensional seismic velocity structure of the northwestern United States. *Geophysical Research Letters*, 35(15), L15304.

Salmi, M. S., Johnson, H. P., & Harris, R. N. (2017). Thermal environment of the Southern Washington region of the Cascadia subduction zone. *Journal of Geophysical Research: Solid Earth*, 122(8), 5852–5870.

Schmandt, B., & Humphreys, E. (2010). Complex subduction and small-scale convection revealed by body-wave tomography of the western United States upper mantle. *Earth and Planetary Science Letters*, 297(3–4), 435–445.

Song, T. R. A., & Helmberger, D. V. (2007). Validating tomographic model with broadband waveform modeling: an example from the LA RISTRA transect in the southwestern United States. *Geophysical Journal International*, 171(1), 244–258.

Soto Castaneda, R. A., Abers, G. A., Eilon, Z. C., & Christensen, D. H. (2021). Teleseismic attenuation, temperature, and melt of the upper mantle in the Alaska subduction zone. *Journal of Geophysical Research: Solid Earth*, 126(7), e2021JB021653.

Syracuse, E. M., van Keken, P. E., & Abers, G. A. (2010). The global range of subduction zone thermal models. *Physics of the Earth and Planetary Interiors*, 183(1–2), 73–90.

Suetsugu, D. (1999). Defocusing of teleseismic P-waves by the Tonga-Kermadec Slab. *Geophysical Research Letters*, *26*(18), 2785–2788.

Takei, Y. (2017). Effects of partial melting on seismic velocity and attenuation: A new insight from experiments. *Annual Review of Earth and Planetary Sciences*, 45, 447–470.

Tang, Y., Obayashi, M., Niu, F., Grand, S. P., Chen, Y. J., Kawakatsu, H., ... & Ni, J. F. (2014). Changbaishan volcanism in northeast China linked to subduction-induced mantle upwelling. *Nature Geoscience*, 7(6), 470–475.

Tromp, J., Komatitsch, D., & Liu, Q. (2008). Spectral-element and adjoint methods in seismology. *Communications in Computational Physics*, 3(1), 1–32.

van Keken, P. E., Hacker, B. R., Syracuse, E. M., & Abers, G. A. (2011). Subduction factory: 4. Depth-dependent flux of H_2O from subducting slabs worldwide. *Journal of Geophysical Research: Solid Earth*, 116(B1), B01401.

van Keken, P. E., Wada, I., Abers, G. A., Hacker, B. R., & Wang, K. (2018). Mafic high-pressure rocks are preferentially exhumed from warm subduction settings. *Geochemistry, Geophysics, Geosystems*, 19(9), 2934–2961.

Vidale, J. E. (1987). Waveform effects of a high-velocity, subducted slab. *Geophysical Research Letters*, 14(5), 542–545.

Wada, I., & Wang, K. (2009). Common depth of slab-mantle decoupling: Reconciling diversity and uniformity of subduction zones. *Geochemistry, Geophysics, Geosystems*, 10(10), Q10009.

Wei, S. S., & Wiens, D. A. (2020). High bulk and shear attenuation due to partial melt in the Tonga-Lau back-arc mantle. *Journal of Geophysical Research: Solid Earth*, 125(1), e2019JB017527.

Wells, R., Bukry, D., Friedman, R., Pyle, D., Duncan, R., Haeussler, P., & Wooden, J. (2014). Geologic history of Siletzia, a large igneous province in the Oregon and Washington Coast Range: Correlation to the geomagnetic polarity time scale and implications for a long-lived Yellowstone hotspot. *Geosphere*, 10(4), 692–719.

Zhan, Z., Helmberger, D. V., & Li, D. (2014). Imaging subducted slab structure beneath the Sea of Okhotsk with teleseismic waveforms. *Physics of the Earth and Planetary Interiors*, 232, 30–35.

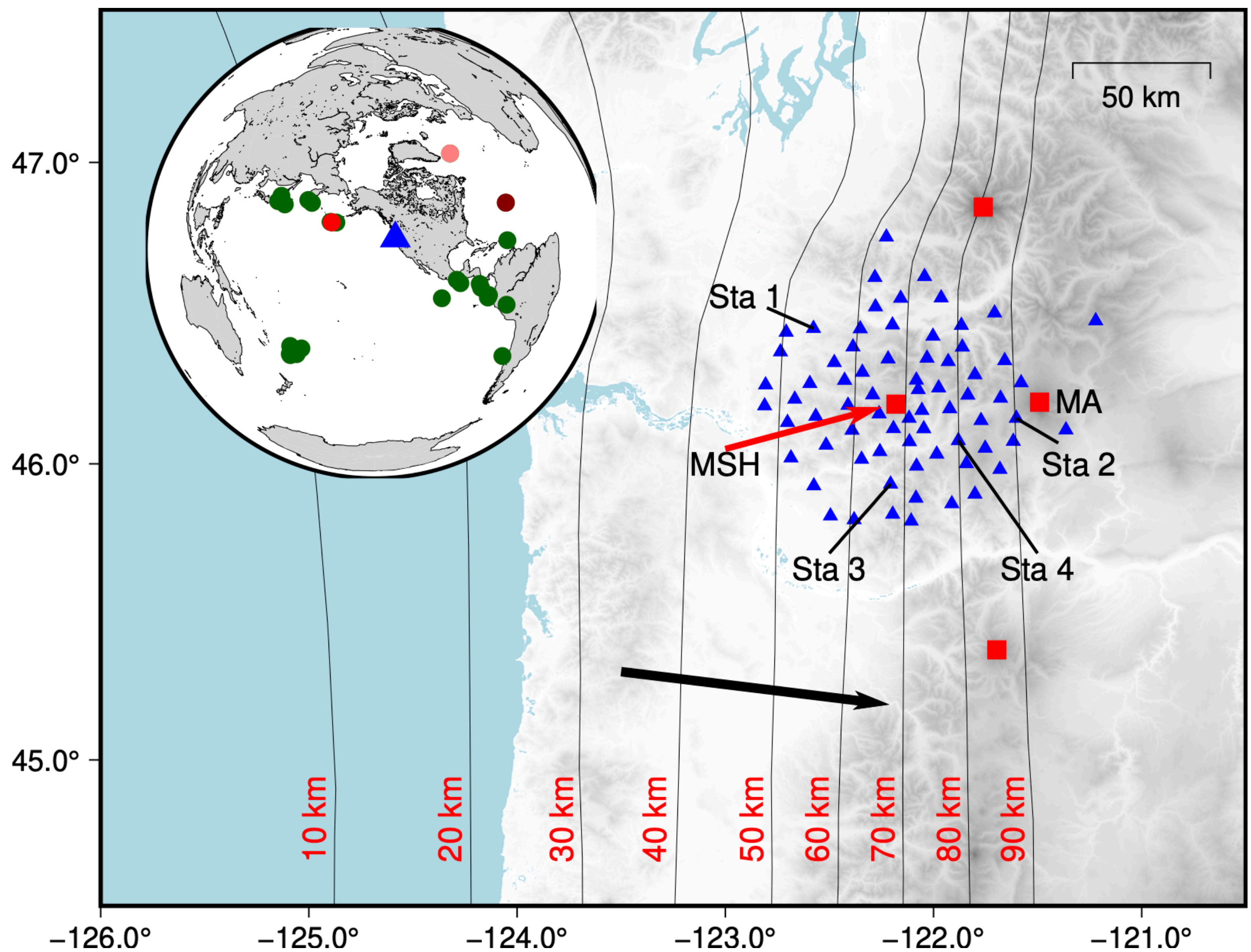

Figure 1. Cascadia subduction zone and the iMUSH array (blue triangles). The red squares show the arc volcanoes. Mount. St. Helens is labeled as MSH and MA is Mount Adams. Thin lines show Juan de Fuca slab depth contours (McCrory et al., 2012). Black arrow shows the subducting direction of the Juan de Fuca slab. Labeled stations discussed in text. Inset shows global view of the iMUSH array (triangle) and the earthquakes (dots) used in this study. The pink dot shows the Greenland earthquake plotted in Fig. 2b. The dark red dot shows the Atlantic Ocean earthquake plotted in Fig. 2c. The red dot shows the Aleutian earthquake in Fig. 2d. Green dots are other earthquakes in this study that amplitude variations are showed in Fig. S1 and S2.

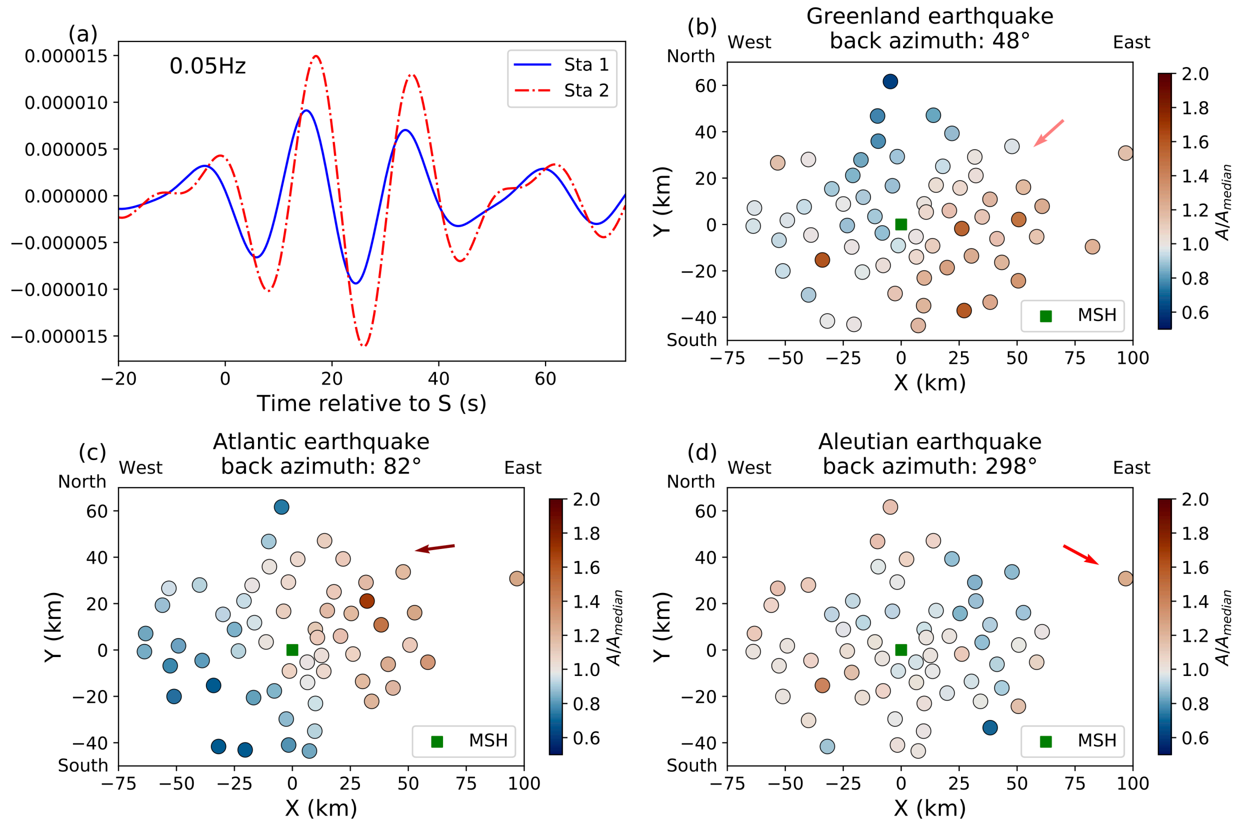

Figure 2. Amplitude variation patterns at 0.05 Hz. (a) Example transverse-component *S*-wave waveforms filtered by a narrowband Butterworth filter at 0.05 Hz with 0.017 Hz halfwidth. The x-axis is time relative to predicted *S* arrivals from the AK135 model (Kennett et al., 1995). **(b)** Amplitude variations of the earthquake near Greenland on the transverse component (pink dot on Figure 1 inset). The amplitudes are normalized to the median amplitude. The origin is Mount St. Helens. Pink arrow shows the wave propagation direction. **(c)** Similar to (b) but for an earthquake located at the center of the Atlantic Ocean on the radial-component (dark red dot on Figure 1 inset). **(d)** Similar to (b) but for an earthquake in the Alaska-Aleutians subduction zone on the transverse component (red dot on Figure 1 inset).

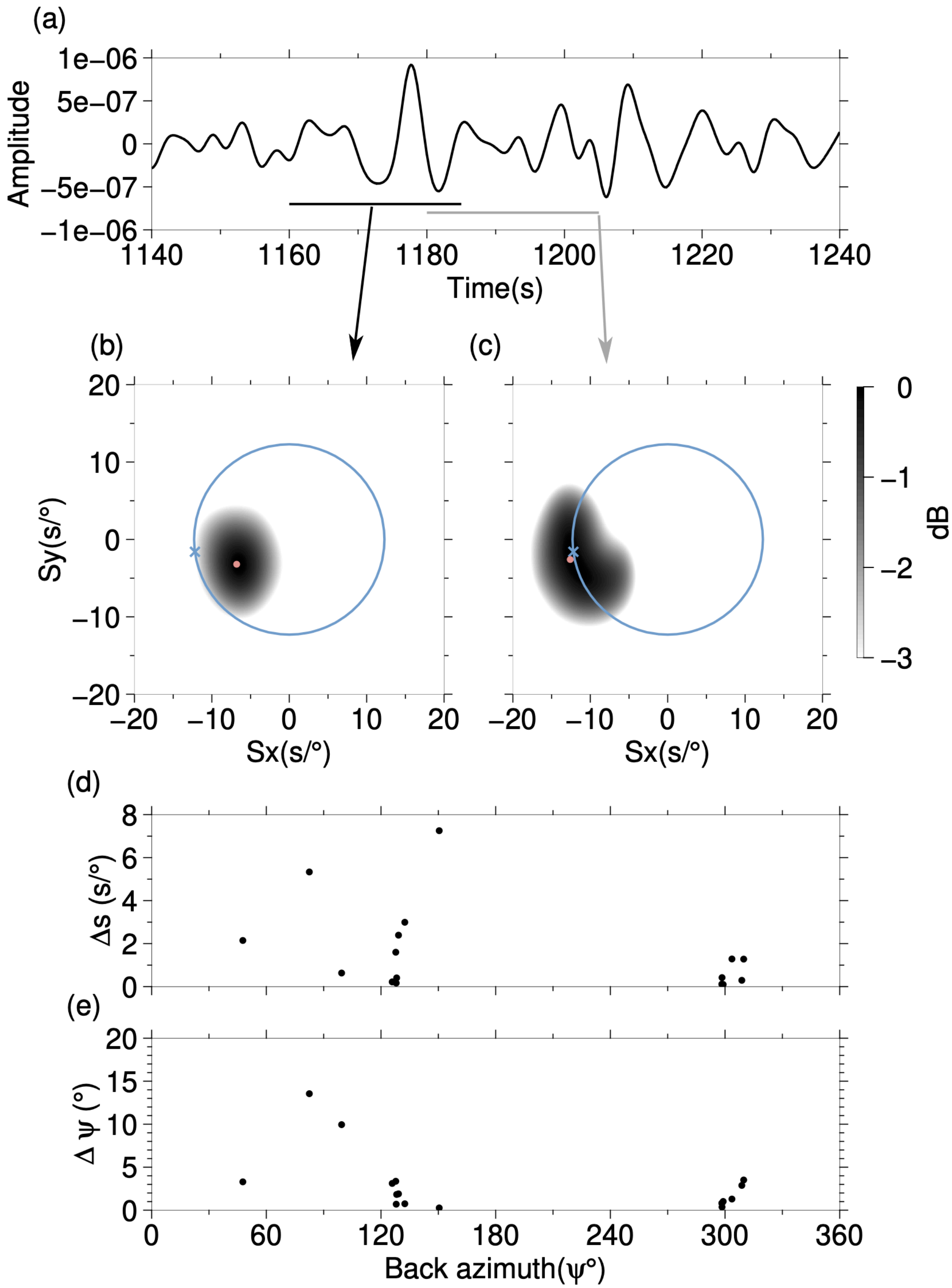

Figure 3. Slowness analysis. (a) Example transverse-component *S*-wave of earthquake at center of Atlantic Ocean, filtered at 0.05–0.3 Hz. **(b)** Beam-forming energy of slowness for the *S* wave

energy over the time intervals marked by black line in (a). The red dot marks the maximum of the power spectrum. Blue cross is the predicted slowness from AK135. Blue circle marks the size of the predicted slowness. **(c)** Similar to (b) but for time interval within the gray line in (a). **(d)** Slowness differences between *S* onset and signals 20 s later for 17 earthquakes. The x-axis is the great-circle back azimuth. **(e)** Difference in back azimuth from *f-k* analysis as a function of great-circle back azimuth.

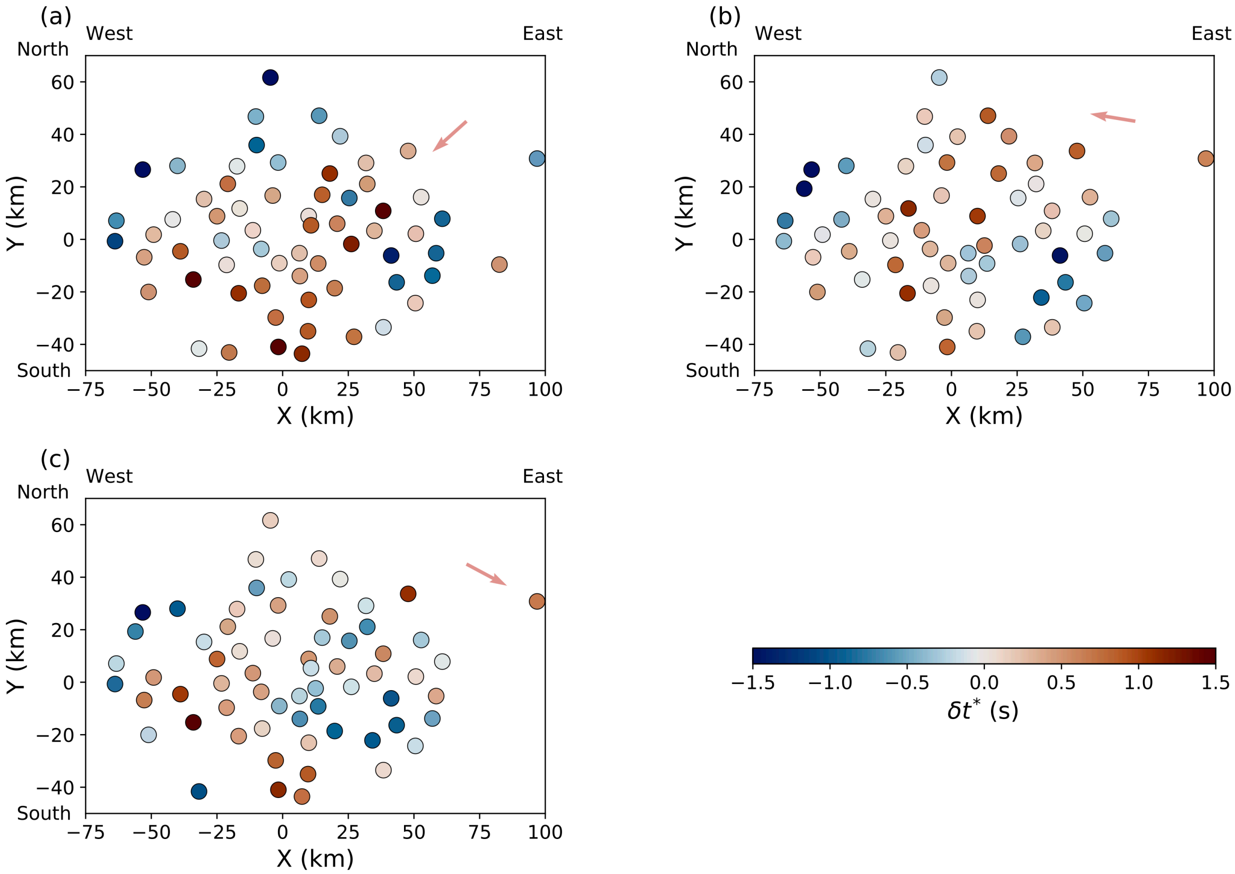

Figure 4. Station–specific *Δt measurements for individual earthquakes. (a)** Earthquake near Greenland with a back azimuth of ~48°. **(b)** Earthquake near Puerto Rico at a back azimuth of ~100°. **(c)** Earthquake in the Aleutians subduction zone at a back azimuth of ~298°. Arrows indicate the directions of wave propagation.

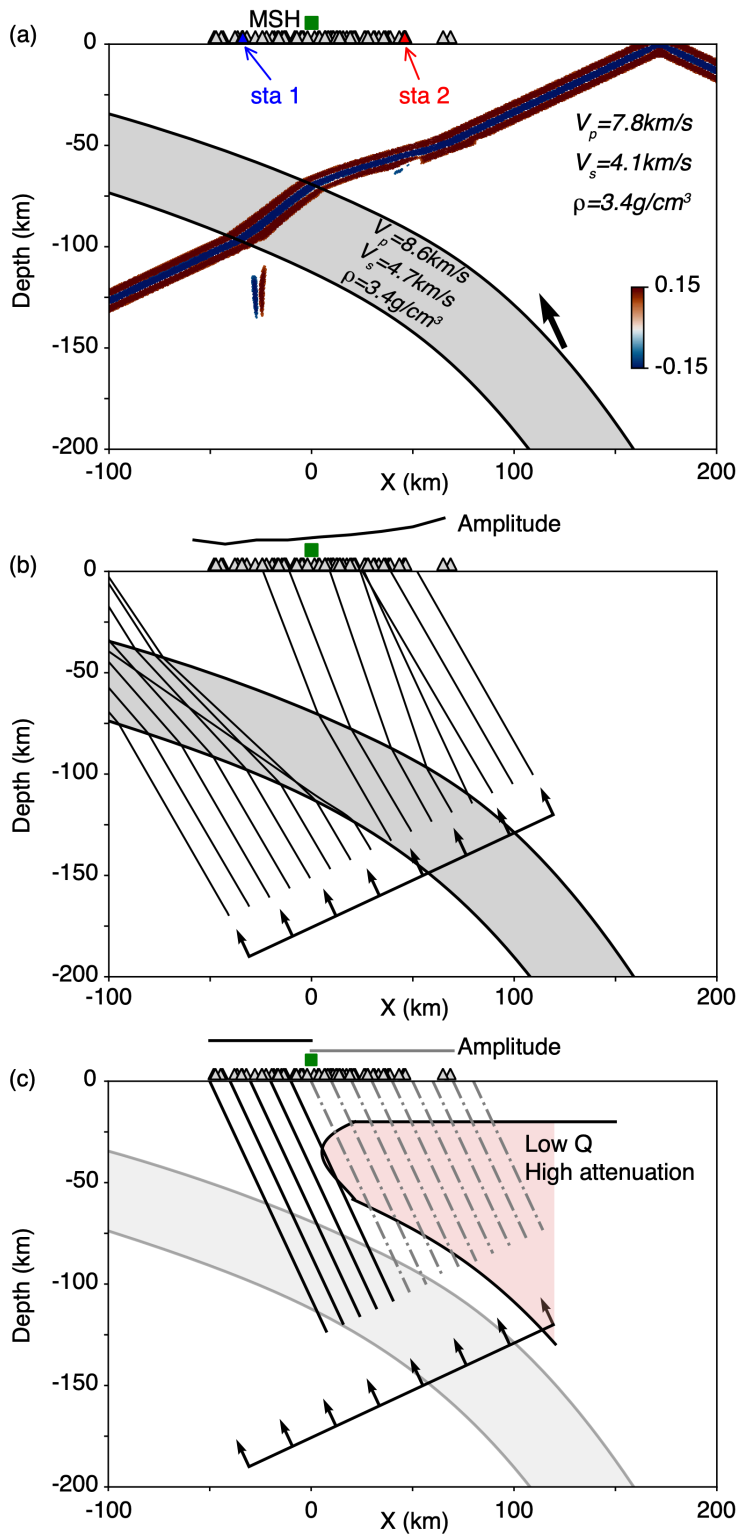

Figure 5. (a) Cascadia Model i, along the black arrow in Figure 1. The subducted plate geometry is described in the text. The x-axis is the distance from Mount St. Helens (MSH, green

square), and the triangles are the iMUSH array. The black arrow indicates the direction of the incident plane wave. The snapshot of the wavefield is shown to exhibit the focusing effects of the subducted slab when the plane wave is incident from the east. Color bar denotes relative wave amplitude. **(b)** Schematic to show how the slab affect wave amplitudes. Regions of wide ray spacing have low amplitudes, and dense ray paths yield large amplitudes. **(c)** Schematic to show how attenuation leads to low amplitudes. Back arc regions have low amplitudes because of the beneath higher temperature mantle wedge. Geometry and other symbols same as (a).

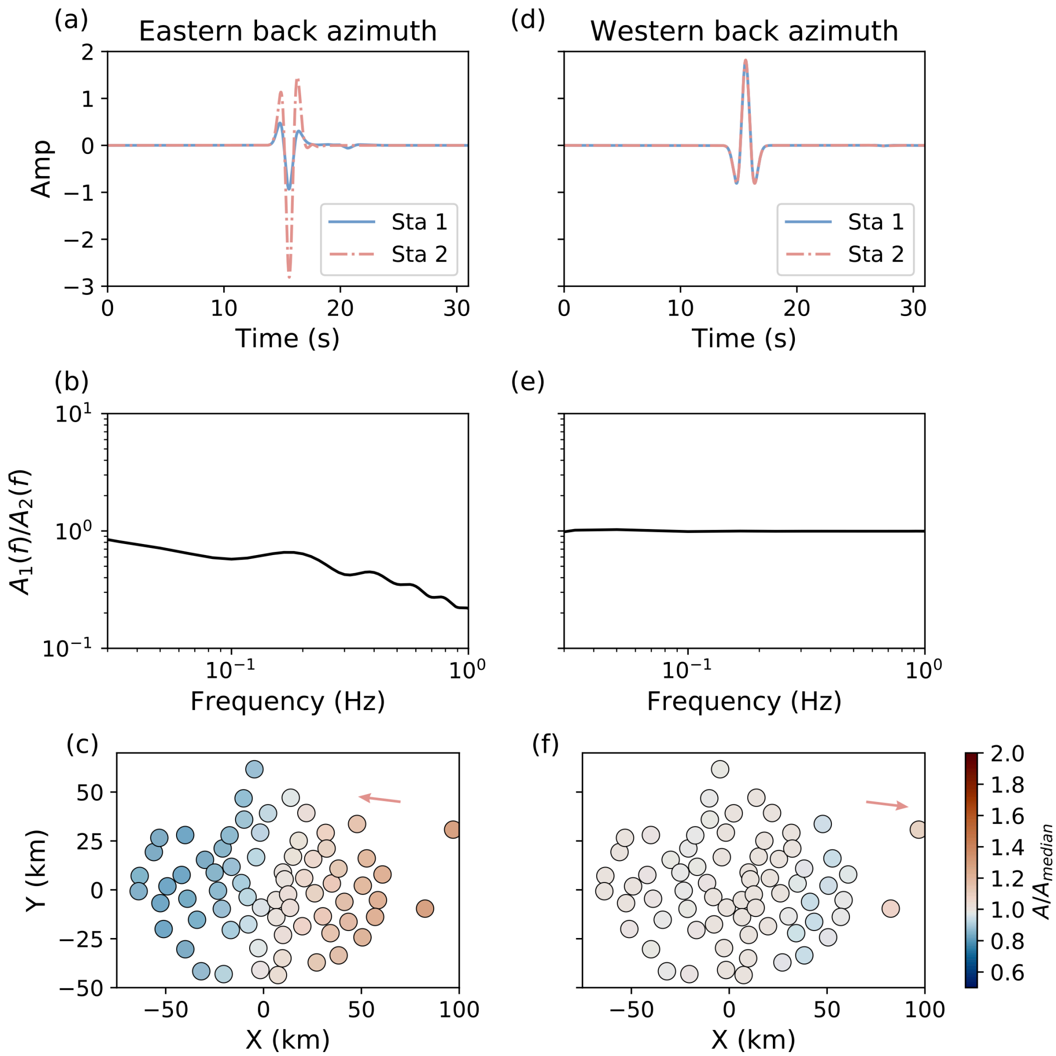

Figure 6. Synthetic results of the simplified Cascadia subduction model. (a) Synthetic waveforms at Sta 1 (blue) and Sta 2 (red) after alignment on the first arrivals. The initial plane wave is incident from the east. **(b)** Amplitude ratio spectra between the synthetic signals shown in (a). **(c)** Amplitude variation of the synthetic waveforms over the iMUSH array. Arrow indicates direction of wave propagation. Waveforms are filtered at 0.05 Hz using the same narrowband filter as the observations in Fig. 2. Origin is Mount St. Helens. **(d)** – **(f)** similar to (a) – (c) but for synthetic wavefields when the initial plane is incident from the west.

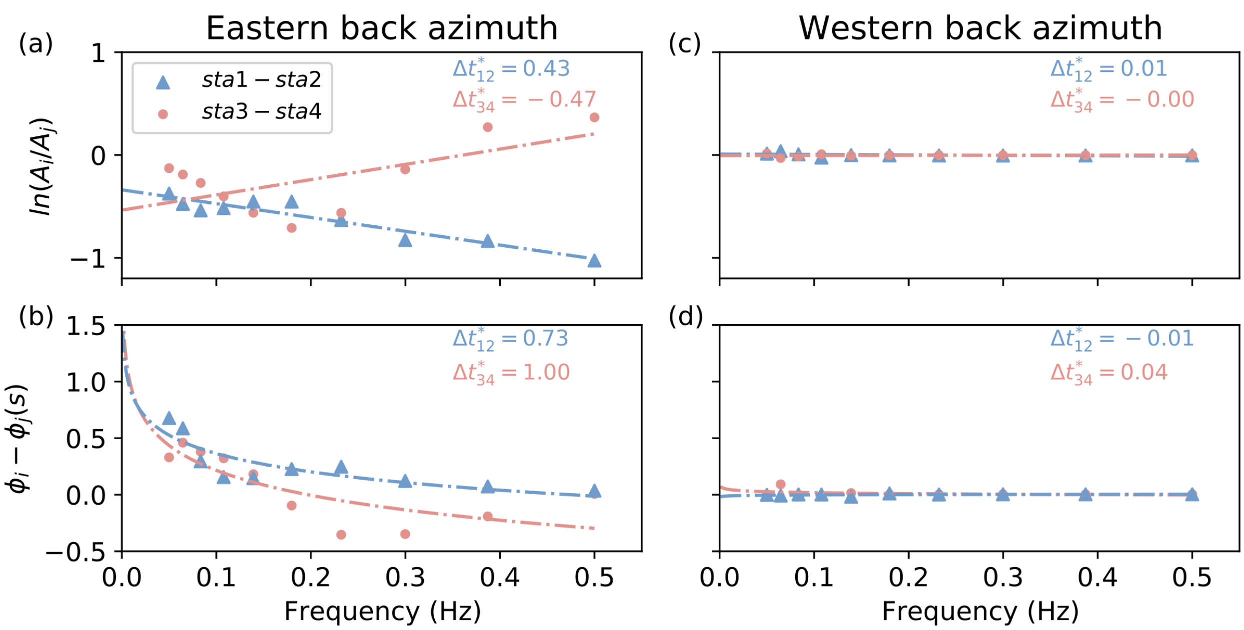

Figure 7. Examples of Δt^* measurements from synthetic waveforms between stations for Model i. (a) Differential Δt^* between station pairs from amplitude ratios of narrow-band filter comb. Blue triangles and red dots are amplitude measurements at each peak frequency for station pair 1-2 and 3-4, respectively. The dashed line is the best fitting differential Δt^* measurement. The initial plane wave is incident from east. **(b)** Similar to (a) but for differential Δt^* from phase shift. Station pair is denoted by color as indicated on label. **(c)** – **(d)** Similar to (a) – (b) but for synthetic waveforms when the initial plane wave is incident from the west.

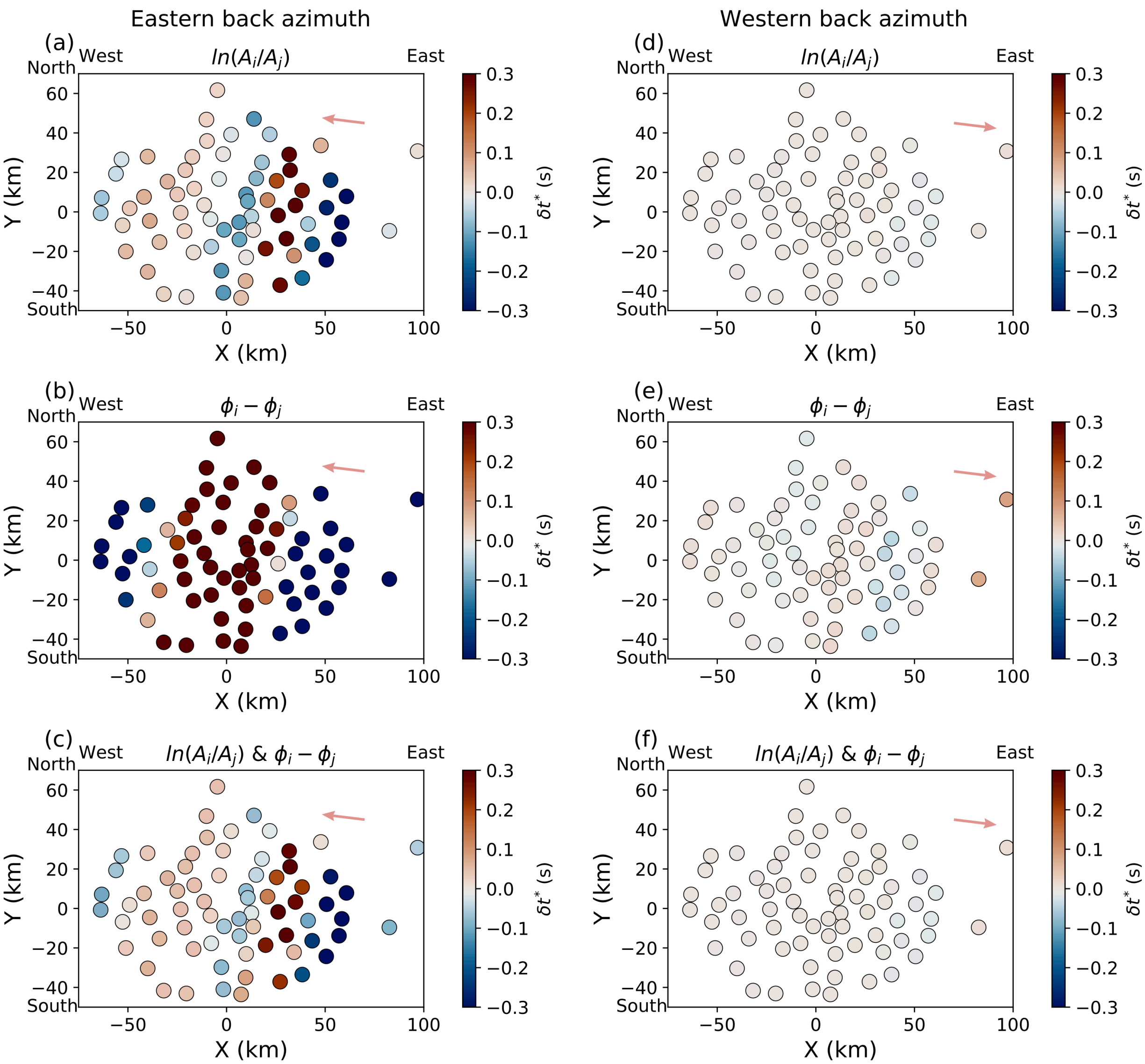

Figure 8. Maps of station–specific Δt^* via linear least-square inversion for synthetics of Model i. (a) – **(c)** show the station–specific Δt^* determined by (a) amplitude ratio only; (b) phase shift only; (c) amplitude ratio and phase shift. The initial plane wave is incident from east; **(d)** – **(f)** Similar to (a) – (c) but for the synthetic waveforms with a western incident plane wave. Arrows show the wave propagation directions.

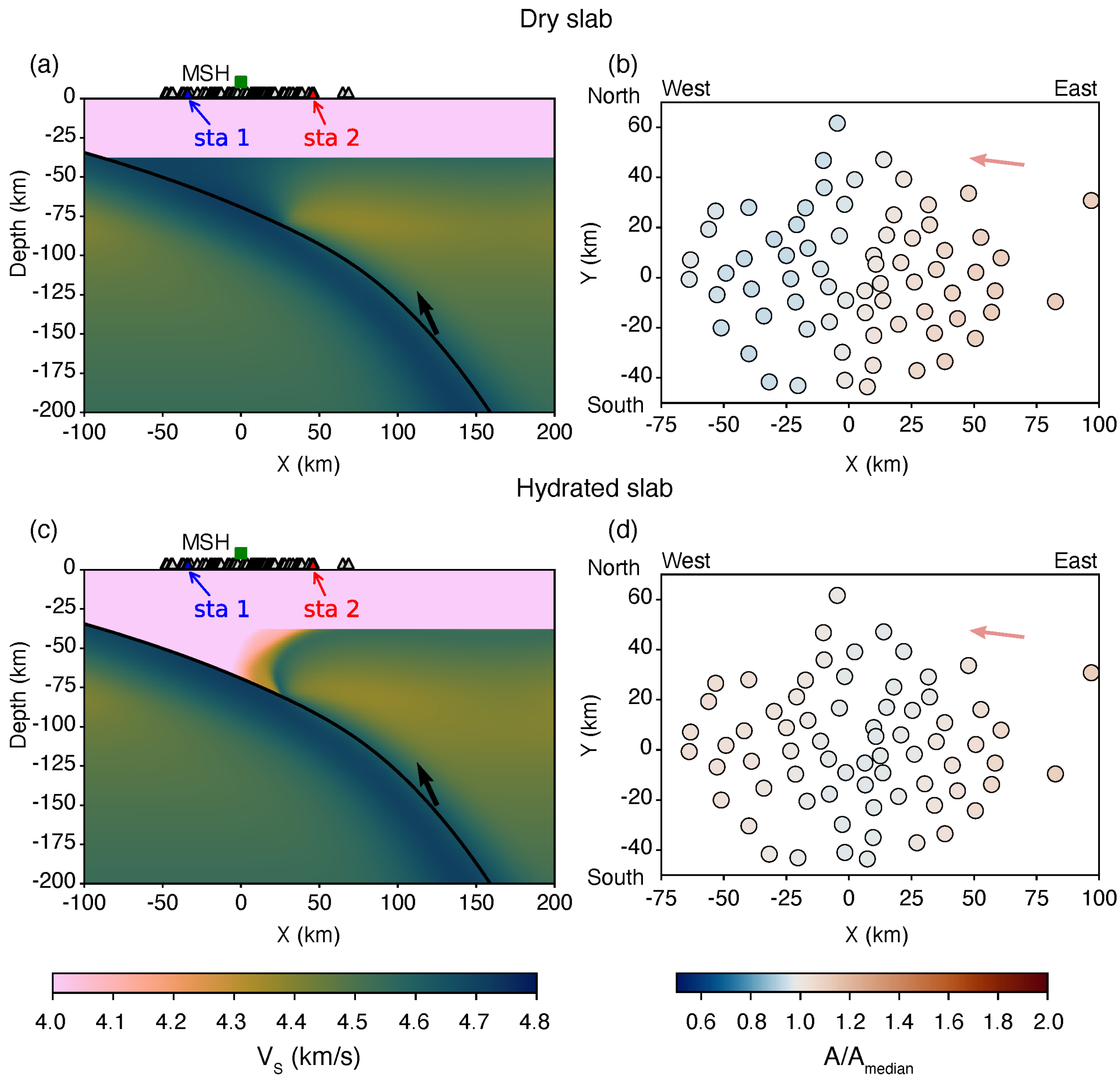

Figure 9. Theoretical Cascadia models and corresponding amplitude variations of synthetic waveforms at 0.05 Hz. (a) Predicted V_s for a dry wedge. Geometry and other symbols same as Figure 5. **(b)** Amplitude variations of synthetic waveforms from the dry wedge model shown in (a). The waveforms are filtered using the same narrow band filter as Fig. 2 and 6c. Arrows show the wave propagation directions. **(c)** Predicted V_s for a fully hydrated forearc mantle wedge. **(d)** Amplitude variations of synthetic waveforms from the hydrated wedge model shown in (c).

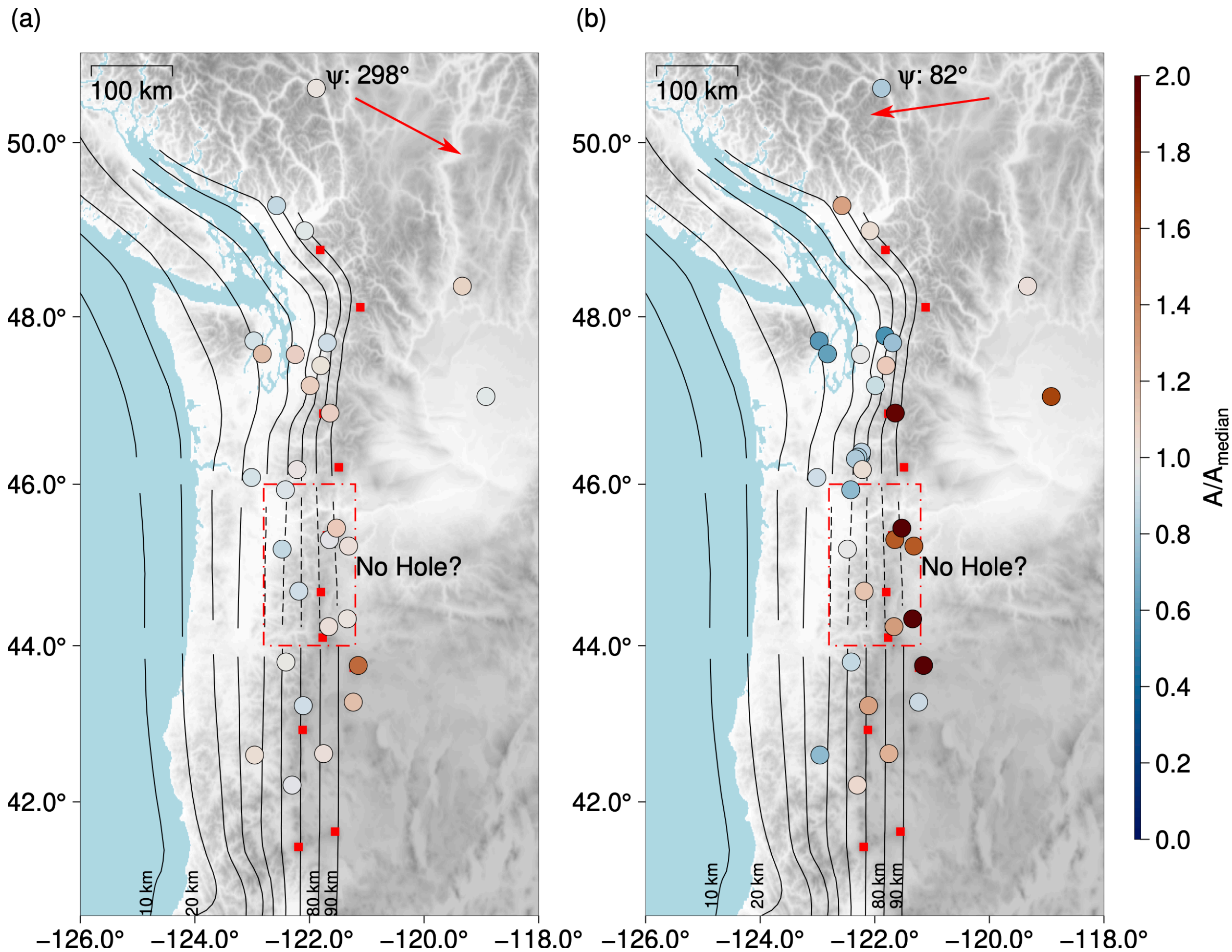

Figure 10. Focusing effects along the arc. (a). Amplitude variation for signals from western back azimuth (same earthquake as in Fig. 2d). **(b)** Amplitude variation for the eastern back azimuth (same earthquake as in Fig. 2c). Circles are broadband stations colored by amplitude anomaly relative to median for that earthquake. Red squares: arc volcanoes; red arrow: wave propagation direction with labled back azimuth. Red dashed rectangle outlines region that of proposed hole in the Juan de Fuca slab (Hawley & Allen, 2019).